

## One Scaffold, Three Binding Modes: Novel and Selective Pteridine Reductase 1 Inhibitors Derived from Fragment Hits Discovered by Virtual Screening<sup>†</sup>

Chidochangu P. Mpamhanga, Daniel Spinks, Lindsay B. Tulloch, Emma J. Shanks, David A. Robinson, Iain T. Collie, Alan H. Fairlamb, Paul G. Wyatt, Julie A. Frearson, William N. Hunter, Ian H. Gilbert, and Ruth Brenk\*

*Division of Biological Chemistry and Drug Discovery, College of Life Sciences, University of Dundee, Dow Street, Dundee DD1 5EH, U.K.*

Received March 31, 2009

The enzyme pteridine reductase 1 (PTR1) is a potential target for new compounds to treat human African trypanosomiasis. A virtual screening campaign for fragments inhibiting PTR1 was carried out. Two novel chemical series were identified containing aminobenzothiazole and aminobenzimidazole scaffolds, respectively. One of the hits (2-amino-6-chloro-benzimidazole) was subjected to crystal structure analysis and a high resolution crystal structure in complex with PTR1 was obtained, confirming the predicted binding mode. However, the crystal structures of two analogues (2-amino-benzimidazole and 1-(3,4-dichloro-benzyl)-2-amino-benzimidazole) in complex with PTR1 revealed two alternative binding modes. In these complexes, previously unobserved protein movements and water-mediated protein–ligand contacts occurred, which prohibited a correct prediction of the binding modes. On the basis of the alternative binding mode of 1-(3,4-dichloro-benzyl)-2-amino-benzimidazole, derivatives were designed and selective PTR1 inhibitors with low nanomolar potency and favorable physicochemical properties were obtained.

### Introduction

Human African trypanosomiasis (HAT<sup>a</sup>), or sleeping sickness, claims the lives of at least 48000 people every year, and about 60 million people in sub-Saharan Africa are at risk of infection.<sup>1</sup> HAT, transmitted by the tsetse fly, is caused by two subspecies of the protozoan parasite *Trypanosoma brucei*.<sup>2,3</sup> The disease progresses in two stages. In the first stage, the parasites proliferate solely within the bloodstream and extracellular tissue space. In the late stage, the central nervous system (CNS) becomes infected, causing symptoms that are characteristic of the disease. If left untreated, HAT is always fatal. Current treatment is hampered by expensive and toxic drugs and emerging resistance and treatment failures complicate the treatment even further.<sup>1</sup> Accordingly, there is an urgent need for the development of safer and more efficient drugs.

Promising targets for new therapeutics are enzymes involved in pterin and folate metabolism.<sup>4</sup> Both pterins and folates are essential for growth in *Leishmania* spp. and related trypanosomatids, yet genes encoding enzymes for de novo synthesis are lacking from their respective genomes.<sup>5</sup> Therefore, trypanosomatids are required to salvage oxidized pteridines such as biopterin and folate and to subsequently reduce them to active cofactors such as tetrahydrobiopterin (H<sub>4</sub>B) and tetrahydrofolate (H<sub>4</sub>F) by means of pteridine reductase

1 (PTR1; EC 1.5.1.33) and the bifunctional enzyme dihydrofolate reductase-thymidylate synthase (DHFR-TS; EC 1.5.1.4 and 2.1.1.45, respectively).<sup>4</sup>

DHFR is a well established drug target for a range of diseases.<sup>6,7</sup> It is therefore surprising that antifolates commonly used as anticancer or anti-infective drugs have not shown equivalent efficacy against *T. brucei* or the related organism *L. major*.<sup>8,9</sup> However, for the latter organism, in which this metabolism has been more extensively investigated, it has been demonstrated that PTR1 not only reduces its principle substrates biopterin and dihydrobiopterin (H<sub>2</sub>B) but also dihydrofolate (H<sub>2</sub>F) and thus circumvents DHFR inhibition.<sup>8,10</sup> It is therefore possible that DHFR and PTR1 have to be inhibited cooperatively in order to produce a therapeutic effect in *L. major*.

Recent evidence indicates that PTR1 might also be a *T. brucei* drug target in its own right. Unlike *L. major ptr1*<sup>−</sup> mutants,<sup>8,11</sup> the bloodstream form of *T. brucei ptr1*<sup>−</sup> mutants is no longer viable in culture medium, suggesting that PTR1 is essential for parasite survival (Sienkiewicz and Fairlamb, unpublished results). This observation prompted us to design *Tb*PTR1 inhibitors to support chemical validation of this potential target and to serve as leads for further development.

Several PTR1 inhibitors are known. Most of them are derived from DHFR inhibitors and contain either a 2,4-diaminopteridine, 2,4-diaminoquinazoline, or 2,4-diaminopyrimidine core (Figure 1).<sup>6,7,12,13</sup> It is therefore not surprising that many PTR1 inhibitors also inhibit human and *T. brucei* DHFR with inhibition constants in the low micromolar to nanomolar range.<sup>12,13</sup> This broad spectrum activity is undesirable both for chemical tools and lead compounds: first, effects due to PTR1 inhibition cannot be distinguished from those due to *Tb*DHFR inhibition and, second, inhibition of

\*To whom correspondence should be addressed. Phone +44 1302 386230. E-mail: r.brenk@dundee.ac.uk.

<sup>†</sup>The crystal structures described in this paper have been deposited with the following PDB ID codes: 2WD7, 2WD8, 3GN1, 3GN2.

<sup>a</sup>Abbreviations: DHFR, dihydrofolate reductase; HAT, human African trypanosomiasis; hDHFR, human DHFR; LmPTR1, *L. major* PTR1; PTR1, pteridine reductase 1; PSA, polar surface area; TbDHFR, *T. brucei* DHFR; *Tb*PTR1, *T. brucei* PTR1.

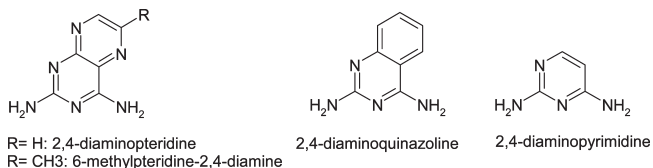


**Figure 1.** Common core structures of PTR1 and DHFR inhibitors.

*h*DHFR will probably lead to undesirable side effects. Moreover, these core structures have a relatively high polar surface area (PSA), ranging from 77 Å<sup>2</sup> to over 100 Å<sup>2</sup>. These types of compounds are therefore less suitable starting points for drug design, particularly when CNS active drugs are required to treat the second stage of the disease.<sup>14</sup>

Crystal structures of *Lm*PTR1 and *Tb*PTR1 have been determined.<sup>15,16</sup> The substrate binding site is a well-defined cleft (Figure 2). In the majority of the crystal structures, the aromatic heterocycle of the ligands is sandwiched between the nicotinamide part of the cofactor NADP<sup>+</sup> and the aromatic moiety of Phe97 (*T. brucei* numbering). Further, the ligands form extensive hydrogen bonds with the cofactor and surrounding amino acids. Even relatively small compounds such as 6-methylpteridine-2,4-diamine (Figure 1) are potent *Lm*PTR1 inhibitors with inhibition constants in the low micromolar range.<sup>13</sup> Collectively, these data suggest that the PTR1 binding pocket is well suited for a fragment-based strategy for hit discovery.

In fragment-based hit discovery, libraries are screened that typically contain molecules with a molecular mass less than 300 Da and with less than three hydrogen-bond donors and six hydrogen-bond acceptors.<sup>17,18</sup> These constraints support the identification of small ligands that bind with a high ligand efficiency and that can be readily optimized to potent drug-like inhibitors. Usually, biophysical methods such as X-ray crystallography, nuclear magnetic resonance (NMR), or surface plasmon resonance (SPR) are used to detect the initial hits, which often have binding affinities in the low millimolar to low micromolar range. In a few cases, also computational methods have been applied to predict fragment binding.<sup>17</sup>

Here, we describe our efforts to support chemical validation of *Tb*PTR1 as a drug target. We report on the discovery of novel *Tb*PTR1 inhibitors using computational fragment screening. The implications of this study for PTR1 inhibitor design and virtual fragment screening are discussed.

## Results

**Virtual Screening.** The following strategy was adopted for virtual screening: (1) selection of an appropriate *Tb*PTR1 structure as template for docking; (2) compilation of a fragment library; (3) docking of the fragment library into the active site of the crystal structure; (4) selection of hits using a combination of pharmacophore-filtering and visual inspection.

Superposition of the available *Tb*PTR1 crystal structures revealed that the binding site is rather rigid, and the observed movements are within the crystallographic coordinate error (Figure 2). The choice of crystal structure should therefore not significantly influence the docking results, and the crystal structure of *Tb*PTR1 in complex with triamterene and NADP<sup>+</sup> (PDB code 3BME) was used as template for virtual screening.

With one exception, in all available *Tb*PTR1 crystal structures, the ligands form a similar hydrogen-bonding

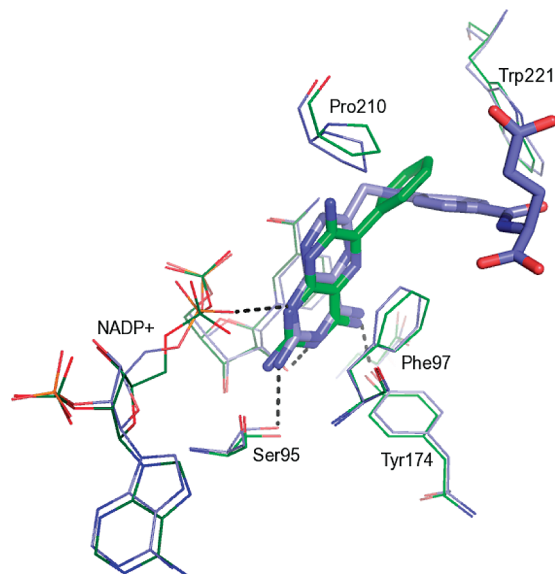


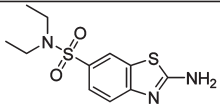
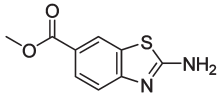
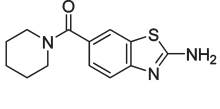
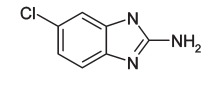
**Figure 2.** Ligands and binding site residues of *Tb*PTR1-methotrexate complex (2C7V, blue carbon atoms) superimposed with those from the triamterene complex (green carbon atoms).

network as observed in the methotrexate and triamterene complexes (Figure 2). However, if in a pharmacophore hypothesis all hydrogen bonds were required, only compounds resembling the known inhibitors and hence with the same problematic physicochemical properties would be retrieved. Therefore, the pharmacophore criteria were relaxed to tolerate all compounds that can interact with the β-phosphate group of the cofactor and can form any of the additional hydrogen bonds.

Recently, we reported on the assembly of a database containing commercially available *lead-like* compounds.<sup>19</sup> To obtain a library of *fragment-like* compounds, this lead-like set was further filtered for compounds containing fewer than 20 heavy atoms, only one or two ring systems, at least one hydrogen-bond donor group, fewer than four rotatable bonds, and a ClogP/ClogD of less than 3.5. By applying these filters, the initial set containing more than 250000 molecules was reduced by approximately 90%.

The resulting fragment library was sequentially docked into the *Tb*PTR1 binding site using DOCK 3.5.54<sup>20,21</sup> A binding mode was generated for 25386 of the 26084 compounds contained in the set. Subsequent filtering of the predicted orientations with the pharmacophore hypothesis described above resulted in 2725 compounds. Compounds containing known PTR1 inhibitor scaffolds (Figure 1) were removed, and the remaining compounds were grouped into five different clusters based on which of the hydrogen bonding interactions previously observed in PTR1–ligand complexes (Figure 2) they fulfilled. The clusters were visually inspected in order to identify compounds representing a diverse set of scaffolds. In addition, the PSA for the scaffold involved in forming the key hydrogen bonds should ideally be less than 70 Å<sup>2</sup>. The selected compounds were subsequently minimized in the binding site while keeping the protein rigid. The criteria for compound purchase were quality of the hydrogen-bond network after minimization and shape complementarity of the ligand and the binding site. Finally, 59 compounds were selected for testing, out of which 45 compounds were available for purchase (Table S1, Supporting Information).

**Table 1.** Docking Results, PTR1 Inhibition Data, and PSA of Virtual Screening Hits<sup>b</sup>

#	Compound	Docking rank (before/after filtering)	$K_i^{\text{app}}$ [ $\mu\text{M}$ ]	Hill slope	PSA [ $\text{\AA}^2$ ] (core <sup>a</sup> /whole molecule)
1		65/43	Compound was not available for purchase		39/76
2		451/255	21.1	0.6	39/65
3		1378/598	141	0.6	39/60
4		97/66	10.6	0.9	55/55

<sup>a</sup>The cores of compounds 1–3 were defined as 2-aminobenzothiazole and of compound 4 as 2-aminobenzimidazole. <sup>b</sup> $K_i^{\text{app}}$  and Hill slopes are averaged over at least two independent measurements.

**Hit Evaluation.** PTR1 inhibition was measured using a novel assay platform recently developed by our group, details of which will be reported in a separate publication. Given the low molecular weight of the screening hits, inhibition was initially tested at 100  $\mu\text{M}$ . Three fragments representing three different chemical scaffolds demonstrated more than 50% inhibition and a further seven compounds from three additional series showed between 30 and 50% inhibition (Table S1, Supporting Information). The hit compounds from the two most potent series of this initial testing containing aminobenzothiazole or aminobenzimidazole cores were further evaluated.

**Aminobenzothiazole Series.** For the aminobenzothiazole series, three compounds were selected for purchase (1–3, Table 1), but only two were available (2 and 3). They have apparent  $K_i$  ( $K_i^{\text{app}}$ ) values of around 21 and 141  $\mu\text{M}$ , giving ligand efficiencies<sup>22</sup> of 0.46 and 0.29 kcal mol<sup>-1</sup>/heavy atom, respectively. The PSA of their core scaffold is 39  $\text{\AA}^2$  (60–65  $\text{\AA}^2$  for the whole molecule), which is 38 to 61  $\text{\AA}^2$  lower than that of the previously known PTR1 inhibitor cores (Figure 1). The pairwise Tanimoto coefficients between previously known PTR1 and DHFR inhibitors scaffolds and these compounds are only 0.1–0.2.

All attempts to cocrystallize these ligands with PTR1 or to soak them into crystals were unsuccessful. This is most likely due to the limited solubility of these compounds. In the proposed binding mode, the ligand is sandwiched between the aromatic moiety of Phe97 and the nicotinamide part of NADP<sup>+</sup>. Further, the ligand forms one hydrogen bond with Ser95 and two with the cofactor (Figure 3).

**Aminobenzimidazole Series.** In the first instance, only one compound containing an aminobenzimidazole scaffold was purchased (4, Table 1). This is the most potent compound discovered from this virtual fragment screen, with a  $K_i^{\text{app}}$  value of 10.6  $\mu\text{M}$  and a ligand efficiency of 0.62 kcal mol<sup>-1</sup>/heavy atom. The compound has a low PSA of 55  $\text{\AA}^2$  and Tanimoto coefficients of 0.3–0.5 when compared with previously known PTR1 and DHFR inhibitor scaffolds.

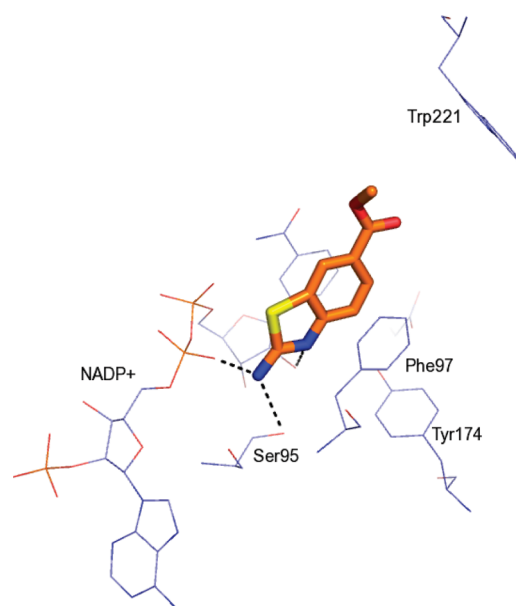


**Figure 3.** Modeled binding mode of 2. The ligand is sandwiched between the aromatic moiety of Phe97 and the nicotinamide part of NADP<sup>+</sup>. Further, the ligand forms hydrogen bonds with Ser95 and the cofactor.

In the proposed binding mode, the ligand is protonated at the nitrogen atom facing the phosphate group of NADP<sup>+</sup> and forms hydrogen bonds with Ser95 and the cofactor (Figure 4b). To initially validate this binding mode in the absence of a crystal structure, close analogues were tested with variations in the six position (5 and 6) and on N1 (7–9, Table 2). Removing the chloro-substituent (5) was accompanied by a more than 20-fold drop in affinity, whereas replacing this substituent with a methylphenyl group (6) resulted in an equipotent compound. Consistent with the proposed binding mode addition of an ethyl group in the N1 (7) position diminished affinity, as this substituent

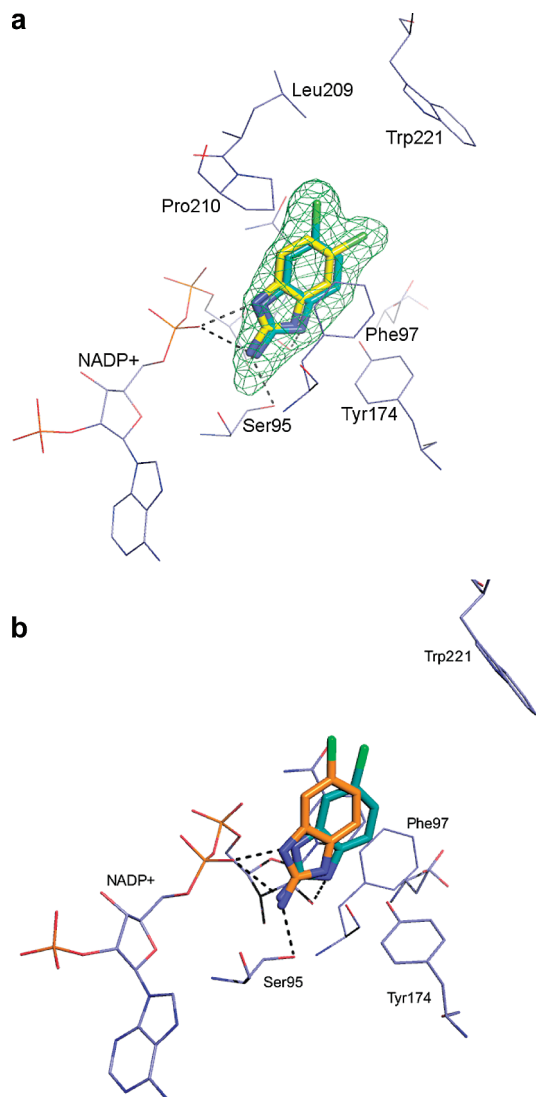


**Figure 4.** (a) View in the binding site of PTR1·4 together with  $F_o - F_c$  omit map (contoured on  $2.0\sigma$ ), which was calculated by omitting the ligand from the final model. The ligand adopts two distinct binding modes. In the major conformation (green carbon atoms), the chloro-substituent packs against Leu209 and Pro210, whereas in the minor conformation (yellow carbon atoms), the chloro atom sits in the open cavity of the active site. (b) Modeled binding mode of 4 (orange carbon atoms) superimposed with the dominant binding mode determined crystallographically (green carbon atoms).

prevents hydrogen-bonding interaction with the phosphate group of NADP<sup>+</sup>. In contrast, larger substituents on this position restored affinity (8) or even led to more than a 20-fold increase in affinity (9) compared to the virtual screening hit.

The binding modes of 4, 5, and 9 were determined using X-ray crystallography (Table 3). Ligand 4 adopts two distinct binding modes with either the N1 or N3 being protonated and forming a hydrogen bond with the phosphate group of the cofactor (Figure 4a). The ratio of these binding modes is 70:30 as estimated by crystallographic  $B$  factors. In the major conformation the chloro-substituent packs against a hydrophobic surface formed by Leu209 and Pro210, whereas in the minor conformation, the chloro atom sits in the open cavity of the active site and forms no van der Waals contacts. The major binding mode resembles closely the best

scoring binding mode of this ligand predicted by DOCK 3.5 (rmsd = 0.95 Å, Figure 4b). The tautomeric form of 4 required in the minor binding mode was present in the docking database but not stored in the final hit list because only the highest scoring version of each compound was kept. The predicted binding mode of this tautomer is within one Å rmsd of the crystallographically determined minor binding mode of 4 (data not shown).

For the unsubstituted fragment 5 only one binding mode was detected (Figure 5). In this binding mode, the ligand forms an edge–face interaction with Trp221 and water mediated hydrogen bonds with the cofactor. The water molecule interacting with the  $\alpha$ -phosphate group of the cofactor occupies a similar position as a water molecule in a *LmPTR1* ligand complex determined previously.<sup>23</sup> The other water molecule has not been observed in any of the previously published structures. Structural water molecules were not considered in the docking protocol and binding mode prediction of 5 failed (rmsd = 3.04 Å).

The most potent ligand 9 adopts a binding mode, which does not resemble any previously observed binding mode (Figure 6). This ligand binds in an area of the active site perpendicular to the canonical binding mode, 3.7 Å away from the nicotinamide moiety of the cofactor. The core occupies a pocket formed by Phe97, Asp161, Met163, Cys168, Phe171, Tyr174, and Gly205. The ligand forms a bidentate interaction with the carboxyl group of Asp161 via the protonated N3 and the 2-amino group, which also hydrogen bonds to the backbone carbonyl of Gly205. The dichloro-phenyl moiety is placed in a pocket defined by the side chains of Val206, Trp221, Leu263, Cys168, and Met163. The pocket is closed by the C-terminal residues His267 and Asp268 from a neighboring subunit. The ligand does not form any hydrogen bonds with the cofactor. The phosphate group of NADP<sup>+</sup> is surrounded by water molecules, which occupy similar positions as in PTR1·5 (Figure 5).

In one monomer (chain D) of the PTR1·9 complex, an additional molecule of 9 was observed in the substrate binding site at lower occupancy. In this binding mode the dichloro-phenyl moiety of the ligand is sandwiched between the nicotinamide part of the cofactor and Phe97 while the benzimidazole part is hydrogen-bonded to the phosphate groups of the cofactor displacing a near-by loop (Leu208–Ala212). This molecule was only modeled with an occupancy of 0.75. The largely hydrophobic nature of the interactions formed within the substrate binding site coupled with the conformational change required for binding suggests that the binding mode can be disregarded as a crystallographic artifact.

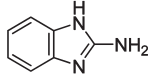
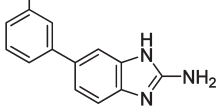
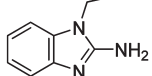
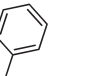
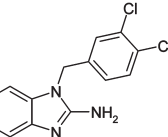
Despite the 1-substituted analogue occupying a very different area of the active site in PTR1 in its main binding mode, the overall rmsd between the main chain atoms of the *TbPTR1*·4 and *TbPTR1*·9 complexes is only 0.25 Å (calculated for chain A), indicating that there is negligible gross conformational change. Considering residues within the active site region the rmsd is 0.43 Å for main chain atoms and 0.65 Å for all atoms, respectively, reflecting the limited nature of ligand induced conformational change. However, the torsion angle defined by CA–CB–CD–CD2 of Trp221 changes from  $-65^\circ$  to  $-75^\circ$  (Figure 6). Without this change, the dichloro moiety of 9 would clash with the tryptophan side chain. In addition, the sulfur atom of Cys168 is shifted by 2 Å in order to accommodate the aminobenzimidazole moiety.



Receptor flexibility was not considered during docking and the docking program was set up to place a ring system close to the phosphate group of the core factor. As a result, a low scoring binding mode was obtained for **9**, which was inconsistent with the above-described pharmacophore hypothesis and which did not resemble the experimentally detected one.

All attempts to determine the binding mode of **6** failed, probably due to the limited solubility of this compound.

**Table 2.** PTR1 Inhibition Data of Readily Available Analogues of 2-Amino-6-chloro-benzimidazole (**4**)<sup>a</sup>

#	Compound	$K_i^{app}$ [ $\mu$ M]	Hill slope
5		288	0.9
6		9.8	1.1
7		>200	
8		23.9	0.7
9		0.4	0.7

<sup>a</sup>  $K_i^{app}$  and Hill slopes are averaged over at least two independent measurements.

Most likely **6** adopts a similar binding mode as **4** with the methylphenyl substituent located in the same area of the binding site as the chloro-substituent of the screening hits. Adopting one of the alternative binding modes would either lead to a steric clash of the aromatic substituent with Trp221 or Phe171.

In summary, depending on the substituents the amino-benzimidazole core adopts three distinct binding modes in the PTR1 active site (Figure 7). Only one of them (**4**) resembles the previously observed binding modes (Figure 2).

**Hit Expansion of Aminobenzimidazole Series.** Crystal structure analysis of *Tb*PTR1·**9** revealed two hydrophobic

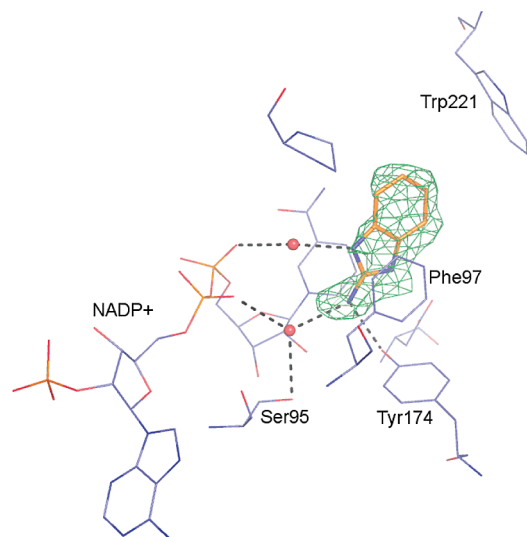


**Figure 5.** Crystallographically determined binding mode of **5** together with  $F_o - F_c$  omit map (contoured on  $2.0\sigma$ ), which was calculated by omitting the ligand from the final model. Two water molecules mediate contacts between the phosphate groups of the cofactor and the ligand.

**Table 3.** Crystallographic Data and Refinement Statistics of *Tb*PTR1–Ligand Complexes<sup>a</sup>

ligand complex	4	5	9	12
Details of Data Collection				
PDB code	2WD7	3GN1	3GN2	2WD8
space group	$P2_1$	$P2_1$	$P2_1$	$P2_1$
unit cell dimensions (Å)	$a = 74.68$ $b = 89.89$ $c = 82.70$ $\beta = 115.48$	$a = 74.64$ $b = 90.41$ $c = 82.64$ $\beta = 115.73$	$a = 74.89$ $b = 90.78$ $c = 82.86$ $\beta = 115.85$	$a = 74.66$ $b = 89.89$ $c = 83.05$ $\beta = 115.54$
resolution range (Å)	30.0–1.90 (2.0–1.90)	30.66–2.00 (2.10–2.00)	67.42–1.60 (1.69–1.60)	30.0–2.10 (2.18–2.10)
observations	147241	341528	522950	118137
unique observations	71041	63246	124512	48991
redundancy	2.1	5.4	4.2	2.4
completeness (%)	91.6 (63.8)	94.8 (89.9)	94.9 (93.7)	84.7 (84.9)
$\langle I/\sigma(I) \rangle$	13.0 (2.4)	9.3 (5.1)	8.3 (2.0)	11.5 (2.43)
$R_{merge}^b$ (%)	5.4 (31.1)	5.1 (13.6)	6.7 (35.9)	9.4 (56.9)
Refinement Statistics				
resolution range (Å)	30.0–1.9	30.66–2.00	67.42–1.60	30.0–2.10
$R$ factor <sup>c</sup> % ( $R_{work}/R_{free}$ )	15.5/20.2	15.5/21.6	14.6/17.8	15.8/22.6
number of atoms <sup>d</sup>	7545/195/88/687	7480/192/20/896	7568/192/95/1272	7453/144/100/733
mean $B$ factor <sup>e</sup> (Å <sup>2</sup> )	26/21/27/35	12/9/26/21	11/8/11/27	30/30/28/41
rms bond length deviation (Å)	0.016	0.014	0.009	0.012
rms bond angle deviation (deg)	1.627	1.473	1.293	1.419

<sup>a</sup> Values between brackets are for the highest resolution shell. <sup>b</sup>  $R_{merge} = \sum |I - \langle I \rangle| / \sum \langle I \rangle$ . <sup>c</sup>  $R$  factor =  $\sum F_o - F_c / \sum F_o$ . <sup>d</sup> Number of atoms of protein, cofactor, ligand, and water molecules, respectively. <sup>e</sup> Mean  $B$  factor for protein, cofactor, ligand, and water molecules, respectively

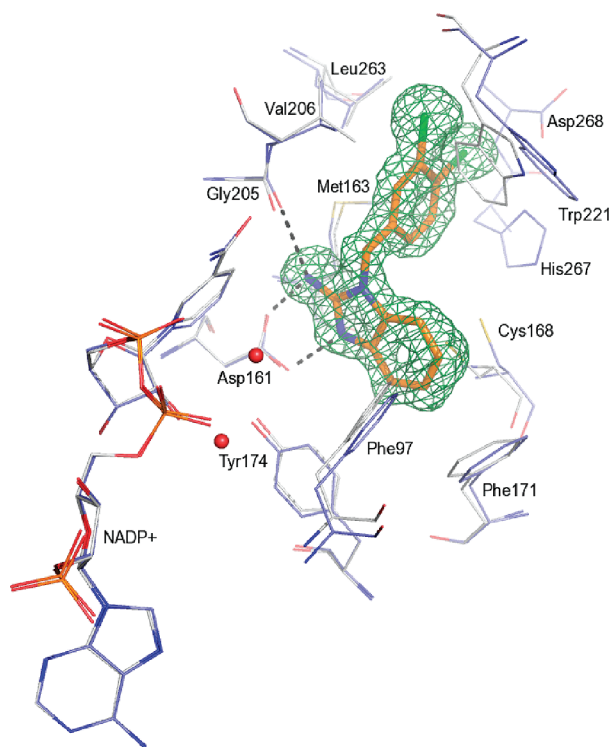


**Figure 6.** Crystallographically determined binding mode of **9** (orange carbon atoms for ligand and blue carbon atoms for protein) superimposed with the receptor conformation used for docking calculations (gray carbon atoms) together with  $F_o - F_c$  omit map (contoured on  $2.0\sigma$ ), which was calculated by omitting the ligand from the final model. To accommodate the ligand in the binding site, the side chain of Trp221 rotated by  $10^\circ$  and the sulfur atom of Cys168 shifted by  $2 \text{ \AA}$ .

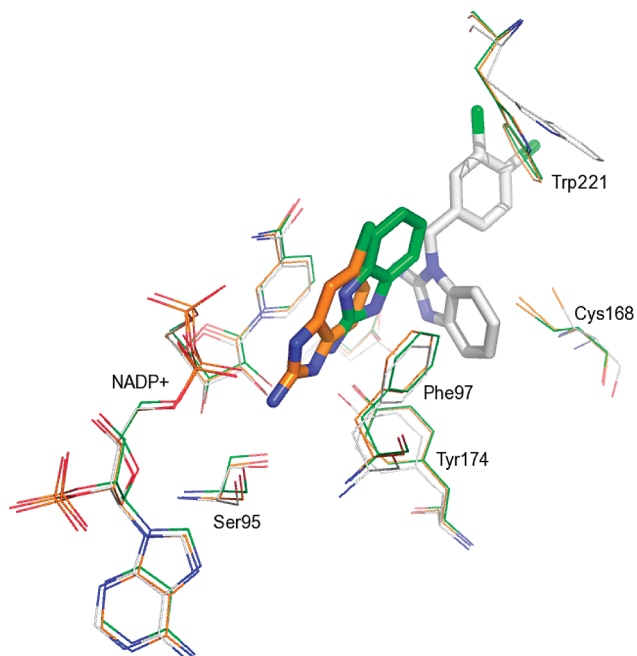


**Figure 7.** Superposition of the crystallographically determined binding modes of **4** (orange carbon atoms), **5** (green carbon atoms), and **9** (gray carbon atoms). Depending on the substituents, the amino-benzimidazole core adopts three different binding modes.

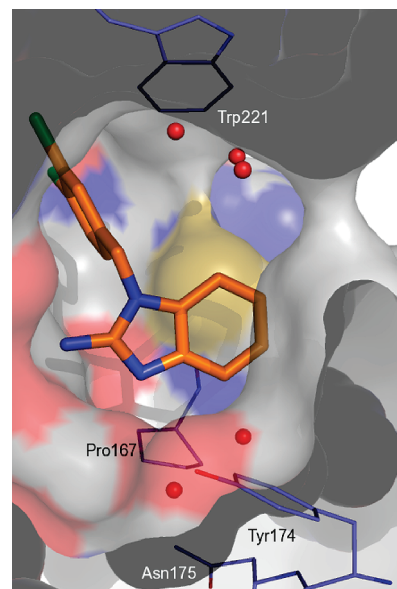


**Figure 8.** Cut-away view of solvent accessible surface of the binding pocket of PTR1·**9**. Two hydrophobic pockets filled with ordered water molecules are close the aminobenzimidazole core of **9**, a smaller pocket bordered by Pro167, Tyr174, and Asn175, and a larger one toward Trp221.

**Table 4.** Hit Expansion of the Aminobenzimidazole Series<sup>a</sup>

#	Structure	$K_i^{\text{app}}$ [ $\mu\text{M}$ ]	Hill slope
10		0.51	1.0
11		0.047	0.7
12		0.007	0.7

<sup>a</sup>  $K_i^{\text{app}}$  and Hill slopes are averaged over at least two independent measurements.

pockets filled with structural water molecules next to the aminobenzimidazole core of **9**: a larger pocket toward Trp221 and a smaller pocket bordered by Pro167, Tyr174, and Asn175 (Figure 8). To improve affinity of the screening hits, derivatives with moieties suitable to fill the larger pocket were designed (Table 4). The 7-chloro-derivative **10** has a  $K_i^{\text{app}}$  of  $0.5 \mu\text{M}$  and is equipotent to **9**. Substituting the chloro-atom with a propoxy-group (**11**) led to a 10-fold increase in potency resulting in a  $K_i^{\text{app}}$  of  $0.05 \mu\text{M}$ . Introducing a phenyl group in this position afforded **12**. With a  $K_i^{\text{app}}$  of  $7 \text{ nM}$  this was the most potent compound in the series.

The crystal structure of *Tb*PTR1·**12** confirmed the modeled binding mode (Table 3, Figure 9). As predicted, the

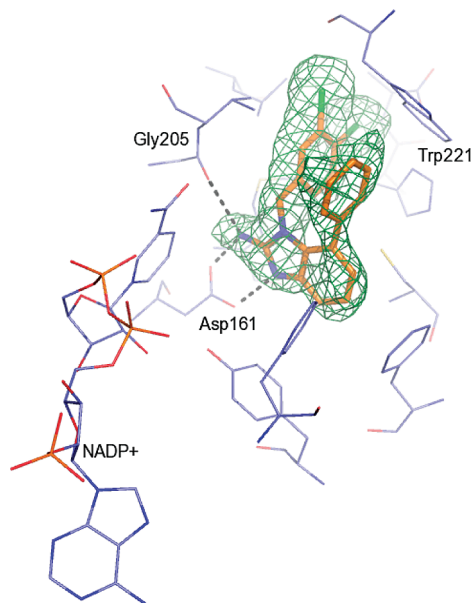


**Figure 9.** Crystallographically determined binding mode of **12** together with  $F_o - F_c$  omit map (contoured on  $2.0\sigma$ ), which was calculated by omitting the ligand from the final model. The phenyl group of the ligand forms an edge-face interaction with Trp221.

inhibitor binds in a similar manner as the parent compound **9** (Figure 6). The additional phenyl ring lies between the side chains of Phe97 and Trp221, forming an edge-face interaction with the latter residue and displacing the structural water molecules, which were found in this area in *TbPTR1-9*.

All compounds showed no significant inhibition of *T. brucei* or human DHFR when tested at concentrations of up to  $30\ \mu\text{M}$  when their  $K_i^{\text{app}}$  values were below  $1\ \mu\text{M}$  and up to  $500\ \mu\text{M}$  for all other compounds. The most potent inhibitor **12** has favorable physicochemical properties for cell and CNS penetration with a molecular weight of 368 Da, a PSA of 55 Å, and an experimentally determined logD of 3.7 units. However, when compound **12** was assayed against *T. brucei* in cell culture, the  $\text{EC}_{50}$  value obtained was only  $10\ \mu\text{M}$ , despite the compound having a  $K_i^{\text{app}}$  of 7 nM against PTR1.

## Discussion

*T. brucei* PTR1 has recently been genetically validated as a drug target for HAT (Sienkiewicz and Fairlamb, unpublished results). Here, we were interested in developing inhibitors of the enzyme to facilitate chemical validation of PTR1 as a drug target for HAT and also to provide drug leads. The leads should have suitable physicochemical properties for further optimization; in the case of stage two HAT, this includes being able to penetrate the CNS.<sup>2,3</sup> One property that is generally needed for such molecules is a low polar surface area ( $<70\ \text{Å}^2$ ).<sup>14</sup> Published inhibitors of PTR1 suffer from low solubility and a relatively high PSA, which reduces the possibility of blood-brain barrier permeation. Furthermore, known PTR1 inhibitors also often inhibit DHFR, which may give rise to toxicity.<sup>12,13</sup> Therefore we aimed to discover novel scaffolds with a low PSA and that inhibit PTR1 and are selective over DHFR. To achieve these goals, we used a virtual fragment screening strategy followed by structure-based ligand design.

We wish to emphasize three results from this study: (1) Virtual fragment screening was successfully applied to discover two novel PTR1 inhibitor scaffolds. (2) X-ray crystallography could confirm the binding mode of one of the inhibitors, but unexpected binding modes were also observed. (3) A highly selective and potent *TbPTR1* inhibitor was designed that can now serve as a chemical tool for target validation.

Our virtual fragment docking protocol identified two novel PTR1 inhibitor scaffolds (Table 1). There is an ongoing debate in the field whether ligand-based or protein-based methods are more effective in virtual screening.<sup>24-27</sup> The scaffolds discovered in this study have a low Tanimoto similarity ( $\leq 0.5$ ) to previously known PTR1 and DHFR inhibitor scaffolds, suggesting that a purely ligand-based screening approach based on 2D similarity would not have been able to identify these compounds.

Fragment docking has been reported for a variety of targets.<sup>17</sup> However, it was noted that the scoring functions that were originally developed for drug-like ligands do not perform equally well for fragment-like ligands.<sup>17</sup> As previous studies demonstrated that pharmacophore constraints are useful tools to overcome these limitations,<sup>28,29</sup> we adopted this strategy and filtered the docking poses using interaction fingerprints.<sup>30</sup> As hypothesized, a better ranking for the putative ligands was achieved (Table 1). However, at least one representative per chemical series ranked already among the top 100 best scoring compounds before reranking. Arguably, in this study, pharmacophore constraints facilitated visual inspection but even without filtering, the same scaffolds would have been discovered.

Knowledge of the binding mode of a fragment is crucial to accelerate optimization of binding affinity.<sup>17,18</sup> One of the binding modes of fragment **4** was correctly predicted by our docking protocol (Figure 4). However, crystal structure analysis revealed that different tautomeric forms of this fragment adopt two distinct binding modes. The second tautomer was present in our database and was predicted to bind in the conformation found in the crystal structure, but because only the highest scoring version of each ligand was saved in the final hit list, this binding mode was not considered when inspecting the virtual screening hits. Removal of the chlorine atom of **4** resulted in ligand **5**, which adopts a further distinct binding mode (Figure 5). In this orientation, two water molecules mediate contacts between the ligand and the protein. Finally, when **4** was substituted on N1 with a dichlorobenzyl moiety (**9**), the protein pocket expanded slightly and the ligand no longer formed hydrogen bonds with the cofactor but bound at a distal site interacting with Asp161 (Figure 6). None of these binding modes was predicted correctly. This points to well recognized issues with molecular docking, which are not specific to fragment docking, such as treatment of tautomeric states, structural water molecules, and protein flexibility.<sup>31</sup> Progress has been made especially in addressing the latter two areas. However, more work remains to be done before these methods can be routinely employed in molecular docking.<sup>32,33</sup>

The different binding modes for the aminobenzimidazole derivatives **4**, **5**, and **9** (Figure 7) are also interesting regarding ongoing discussions on if, or how, the binding modes of the ligands change when going from fragment to lead and drug.<sup>17</sup> Babaoglu and Shoichet deconstructed a  $\beta$ -lactamase inhibitor into four fragments and found different binding modes for each of them.<sup>34</sup> However, only one of these fragments contained the same key recognition element that was also present



in the parent molecule. This might potentially explain the multiple observed binding modes in their case.<sup>35</sup> Here, all three ligands contain the same key recognition element, the benzimidazole motive, but due to the substitution patterns of **5** and **9**, their binding modes are mutually exclusive. A substituent in N1-position in the binding orientation of **5** would lead to a steric clash with the phosphate group of the cofactor (Figure 4), while substituting the 8-position in the binding mode of **9** would lead to a steric clash with Phe174 (Figure 6). The smaller fragment **4** could theoretically adopt either of these binding modes. Instead, the ligand binds in a third orientation with water-mediated contacts to the phosphate group of the cofactor and an edge–face interaction with the aromatic side chain of Trp221. The later interaction has been observed to be important to improve binding affinity of unrelated PTR1 inhibitors (unpublished results) and might be the driving force for this orientation.

Chemical validation of *Tb*PTR1 as a drug target for HAT is still outstanding. To this end, potent and selective PTR1 inhibitors are needed. Here, we focused on optimizing one of the two scaffolds that were discovered by virtual fragment screening. Out of the three possible binding modes that the aminobenzimidazole derivatives can adopt in the binding pocket, we chose the binding mode of **9** as a start point for hit expansion. Because of pronounced differences between DHFR and PTR1 in the area of the active site where this inhibitor binds, this strategy should lead to highly selective PTR1 inhibitors.

To optimize the submicromolar activity of **9** (Table 2), we sought to fill the hydrophobic pocket close to Trp221 identified by the analysis of the crystal structure *Tb*PTR1·**9** (Figure 8). Indeed, the subsequently synthesized phenyl-derivative **12** was more than 100-fold more active than **9** and highly selective over both human and *T. brucei* DHFR. Its measured logD is with 3.7 units in a range that suggests that this compound should be membrane permeable. In addition, this ligand has a PSA of only 55 Å<sup>2</sup>, which is well in the required range for compounds to pass the blood–brain barrier, a property required to treat the second stage of African sleeping sickness.<sup>2,3,14</sup> Consequently, the ligand should be a valuable tool to support chemical validation of *Tb*PTR1 as drug target. Somewhat surprisingly, this ligand poorly inhibited *T. brucei* cell growth in culture, having an EC<sub>50</sub> value of only 10 μM. Similar results have been obtained with PTR1 inhibitors containing different chemical scaffolds (unpublished data). At the moment, it is unclear what the reasons are for lack of translation of potent inhibition of PTR1 to an antiproliferative activity against the parasites in culture. Studies are underway to investigate this further.

## Methods

**Preparation of Small Molecule Databases.** An in-house database containing over 2.2 million commercially available compounds was constructed and associated physicochemical descriptors along with flags for unwanted groups were calculated as described previously.<sup>19</sup> For molecular docking, in house python scripts based on OpenEye's OEToolkit (Openeye, Santa Fe, NM) were used to generate common tautomeric states and to charge small molecules, whereas for acidic and basic groups with estimated pK<sub>a</sub> values between 5 and 9 both, the neutral and charged forms were stored. Three dimensional conformations were calculated using Corina (Molecular Networks, Germany), and low energy conformers were sampled using Omega (Openeye). Partial atomic charges and desolvation energies for the

transfer from high-dielectric media (simulated as water) to low dielectric media (simulated as cyclohexane) were computed using AMSOL (<http://comp.chem.umn.edu/amsol/>) with the same settings as used previously.<sup>36</sup> The generated molecules were stored in a hierarchical whereas each ring fragment of each database molecule was sequentially used as anchor to align the conformers resulting in several anchors for molecules containing multiple ring fragments.<sup>20</sup>

**Receptor Preparation.** The crystal structure of *Tb*PTR1 in complex with triamterene and NADP<sup>+</sup> (PDB code 3BME) was chosen as the receptor for this study. Polar hydrogen atoms were added and their positions were minimized using the MAB force field<sup>37,38</sup> as implemented in Moloc (Gerber Molecular Design, Switzerland) with the ligand present in order to obtain a hydrogen-bonding network optimized for ligand binding. Subsequently, all crystallographic water molecules and the inhibitor were removed. Amber charges were assigned to the protein atoms and AMSOL charges to the cofactor. Spheres were manually placed in the binding site in the area that was occupied by the pyrido[3,4-*b*]pyrazine-2,5,7-triamine part of the ligand and used as receptor matching positions for docking and to lower the effective dielectric in the bindings. Grids to store information about excluded volumes, electrostatic and van der Waals potential, and solvent occlusion were calculated as described earlier.<sup>36</sup>

**Molecular Docking.** DOCK 3.5.54 was used to dock small molecules flexibly in to the active site of *Tb*PTR1.<sup>20,21</sup> The following settings were chosen to sample ligand orientations: ligand and receptor bins were set to 0.5 Å, overlap bins were set to 0.4 Å, the distance tolerance for matching ligand atoms to receptor matching sites ranged from 1.1 to 1.2 Å. Each docking pose which did not place any atoms in areas occupied by the receptor was scored for electrostatic and van der Waals complementarity<sup>20</sup> and penalized according to its estimated partial desolvation energy (B. Shoichet, unpublished). For each compound, only the best-scoring database representation (tautomer, protonation state, multiple ring alignment) was stored in the final docking hit list.

**Pharmacophore-Based Filtering of Docking Poses and Visual Inspection.** After analysis of available crystal structures, key interactions in the pteridine binding site were identified as  $\pi$ -stacking interactions to Phe97 and the nicotinamide part of the cofactor NADP<sup>+</sup>, an essential hydrogen bond to one of the oxygen atoms of the phosphate group of the cofactor, and optional hydrogen bonds to either the hydroxyl group of Ser95, Tyr174, or the ribose part of the cofactor (Figure 2). To filter and cluster the docking poses, the hydrogen bond interactions identified were encoded into interaction fingerprints.<sup>30</sup> A hydrogen bond interaction was assumed when a distance of <3.5 Å was measured between the protein atoms potentially involved in hydrogen bonds described above and a heteroatom of the ligand. Compounds passing this filter step were minimized in the binding site using the MAB force field<sup>32,33</sup> as implemented in Moloc. Subsequently, the obtained binding poses were visually inspected and representative compounds still maintaining the required hydrogen-bond network were short-listed for purchase.

**Structure-Based Ligand Design.** Starting with the crystal structure of *Tb*PTR1·**9**, potential derivatives of the hit compound that bear moieties suitable to fill the hydrophobic pocket next to Trp221 (Figure 8) were constructed using Moloc. Subsequently their binding modes were minimized using the MAB force field and promising compounds were selected for synthesis

**Calculation of Tanimoto Coefficients and Polar Surface Area.** Tanimoto coefficients were calculated using Sybyl (Tripos, St. Louis, MO) based on standard Tripos fingerprints. Topological polar surface areas were calculated using a Python script provided by Openeye based on a previously published method.<sup>39</sup>

**PTR1 and DHFR Activity Assays.** Compounds **2–4** and **8–9** were purchased from Asinex, compound **5** from Sigma-Aldrich,



and compound **7** from Chemdiv. Purity (>90%) and identity of these compounds was confirmed by LCMS. Compound **6** was available in-house from a different chemistry program and its synthesis will be reported elsewhere. The synthesis for compounds **10–12** is reported below.

*TbPTR1* and DHFR activity was measured in 96-well microtiter plates via reduction of cytochrome *c* (*cytc*) as a result of the enzymatic production of tetrahydrobiopterin ( $H_4B$ ) and tetrahydrofolate ( $H_4F$ ), respectively. In brief, *TbPTR1* activity was assayed in a buffer containing 20 mM sodium citrate, 1 mM EDTA,  $H_2B$  (0.35  $\mu M$ ), *cytc* (81  $\mu M$ ), and NADPH (100  $\mu M$ ) at pH 6.0; DHFR was assayed in 20 mM sodium citrate, 1 mM EDTA,  $H_2F$  (4.4  $\mu M$ ), *cytc* (81  $\mu M$ ), and NADPH (100  $\mu M$ ) at pH 7.4. Enzyme activity was monitored by reading absorbance at 550 nm within the linear phase of reaction. Full details of this method will be reported in a separate publication.  $K_i^{app}$  values were calculated using a modified Morrison equation.<sup>40</sup>

**Protein Crystallization, Data Collection, and Structure Solution.** *TbPTR1* was purified and crystallized as described previously.<sup>15</sup> In short, *TbPTR1* was concentrated to 6 mg/mL in 20 mM Tris-HCl pH 8.0. Ligands were solubilized to a concentration of 200 mM in DMSO. The ternary complex of *TbPTR1* with cofactor and ligand was prepared by incubating the protein solution (6 mg/mL) with 2 mM of the ligand, 1 mM  $NADP^+$ , and 20 mM dithiothreitol in 20 mM Tris-HCl pH 8.0 on ice for 30 min prior to crystallization. Crystallization was carried out by the vapor diffusion method by mixing 2  $\mu L$  of the protein solution with 2  $\mu L$  of the reservoir solution and incubating the drops over 100  $\mu L$  of the reservoir in sitting drop plates. The reservoir solution consisted of 1.5–3.0 M sodium acetate and 0.1 M citrate buffer pH 4.5–6.0. Diffraction quality crystals were obtained after 2–3 days at 18 °C.

Diffraction data for the complexes with **4**, **5**, and **12** were measured using a rotating anode X-ray source (Rigaku Micro-max 007) and an image plate detector (Rigaku R-AXIS IV<sup>++</sup>) and for the remaining complex at beamline ID23-1 at the European Synchrotron Radiation Facility (ESRF) in Grenoble, France. Crystals were prepared for data collection by transferring them through a cryoprotection solution of mother liquor with 20% glycerol added and then flash frozen in a stream of gaseous nitrogen at  $-173$  °C. Data were integrated and scaled using MOSFLM<sup>41</sup> and SCALA<sup>42</sup> from the CCP4<sup>43</sup> suite of programs, except for complex *PTR1*·**12**, for which the HKL suite was used.<sup>44</sup>

Molecular replacement as implemented in MOLREP<sup>45</sup> was used to solve the structure using the protein chains from the *TbPTR1*·methotrexate complex<sup>15</sup> (PDB 2C7V) as the starting model. After the molecular replacement step, a round of rigid-body refinement was carried out using REFMAC5.<sup>46,47</sup> Ligand models and associated topology files were created with PRODRG<sup>48</sup> and were built into  $F_o - F_c$  electron density maps using COOT.<sup>49</sup> Further rounds of restrained refinement were carried out using REFMAC5 and manual alteration of the models, including addition of solvent molecules using COOT.

Figures of protein–ligand complexes were produced using PyMOL (DeLano Scientific, Palo Alto, CA).

**Synthesis of Amino-benzimidazole Analogues.** <sup>1</sup>H NMR spectra were recorded on either a Bruker Avance DPX 500 or on a Bruker Avance 300 spectrometer. Chemical shifts ( $\delta$ ) are expressed in ppm. Signal splitting patterns are described as singlet (s), broad singlet (bs), doublet (d), triplet (t), quartet (q), multiplet (m), or combinations thereof.

Low resolution electrospray (ES) mass spectra were recorded on a Bruker MicroTof mass spectrometer, run in positive ion mode, using either methanol, methanol/water (95:5), or water/acetonitrile (1:1) and 0.1% formic acid as the mobile phase. High resolution electrospray measurements were performed on a Bruker MicroTof mass spectrometer.

LC-MS analysis and chromatographic separations were conducted with a Bruker MicroTof mass spectrometer using an

Agilent HPLC 1100 with a diode array detector in series. The column used was a Phenomenex Gemini C18 column, 50 mm  $\times$  3.0 mm, 5 mm particle size. The following method was used: mobile phase, water/acetonitrile + 0.1% HCOOH 80:20 to 5:95 gradient over 3.5 min, and then held at for 1.5 min; flow rate 0.5 mL/min.

All compounds exemplified had a measured purity of greater than 95% on this analytical HPLC-MS system (TIC and HPLC UV). HPLC retention times and  $M^+$  data are given below to substantiate the purity and integrity of the compounds. <sup>1</sup>H NMR also confirmed compound identity and purity (wrt other organic components being absent).

Thin layer chromatography (TLC) was carried out on Merck silica gel 60 F254 plates using UV light and/or  $KMnO_4$  for visualization. TLC data are given as the  $R_f$  value with the corresponding eluent system specified in brackets. Column chromatography was performed using RediSep 4 or 12 g silica prepacked columns.

All reactions were carried out under dry and inert conditions unless otherwise stated.

**7-Chloro-1-(3,4-dichlorobenzyl)-1H-benzo[d]imidazol-2-amine (10).** 7-Chloro-1H-benzo[d]imidazol-2-amine (**16**) (200 mg, 1.19 mmol), potassium hydroxide flakes (100 mg, 1.79 mmol), and 3,4-dichlorobenzyl chloride (244 mg, 1.25 mmol) were stirred in 15 mL ethanol at 20 °C for 48 h. The solution was then concentrated by removing the ethanol and diluted with 40 mL ethyl acetate and washed with sodium bicarbonate solution (1  $\times$  20 mL), water (1  $\times$  30 mL), and brine (2  $\times$  20 mL). The organic layer was dried with magnesium sulfate and concentrated to remove the ethyl acetate to afford a cream-colored solid. Compound **10** was the more polar product obtained purified by flash column chromatography (10% methanol/ dichloromethane eluent), yielding compound **10** as a white solid (68 mg, 17% yield). <sup>1</sup>H NMR and LCMS confirmed purity at >98%.

The relative <sup>1</sup>H NMR signal for the  $CH_2$ -dichlorobenzyl protons at 5.54 ppm, versus 5.28 ppm for 4-isomer, agrees with the expected shift for a 7-substituted  $N^1$ -benzylated benzimidazole versus a 4-substituted benzimidazole.<sup>50</sup>

<sup>1</sup>H NMR (500 MHz, DMSO):  $\delta$  = 5.54 (2H, s,  $CH_2$ ), 6.78 (2H, s,  $NH_2$ ), 6.83 (1H, m, ArH), 6.95 (1H, dd ( $J$  = 2.1 Hz,  $J$  = 8.4 Hz) ArH), 6.97 (1H, t ( $J$  = 7.9 Hz) ArH), 7.15 (1H, dd ( $J$  = 0.9 Hz,  $J$  = 7.8 Hz), ArH), 7.31 (1H, s, ArH), 7.61 (1H, d ( $J$  = 8.3 Hz), ArH).

LCMS ( $ES^+$ ):  $m/z$  (%) 327 ( $M + H^+$ ), retention time 0.9 min.

HRMS ( $ES^+$ ): calcd for  $(C_{13}H_{11}Cl_3N_3 [M + H]^+)$  326.0013, found 325.9998 (4.47 ppm).

**7-(*n*-Propyloxy)-1-(3,4-dichlorobenzyl)-1H-benzo[d]imidazol-2-amine (11).** 7-(*n*-Propyloxy)-1H-benzo[d]imidazol-2-amine (**13**) (250 mg, 1.31 mmol), potassium hydroxide flakes (110 mg, 6.28 mmol), and 3,4-dichlorobenzyl chloride (269 mg, 1.38 mmol) were stirred in 10 mL ethanol at 20 °C for 48 h. The reaction was worked up as described for compound **10**, and columned. Compound **11** was the more polar product obtained purified by flash column chromatography (10% methanol/ dichloromethane eluent), yielding compound **11** as a white solid (90 mg, 20% yield). <sup>1</sup>H NMR and LCMS confirmed purity at >98%.

Absolute regiochemistry of compound **11** was confirmed by the relative <sup>1</sup>H NMR signal for the  $CH_2$ -dichlorobenzyl protons at 5.48 ppm, versus 5.08 ppm for 4-isomer. This agrees with the expected shift for a 7-alkoxy substituted  $N^1$ -benzylated benzimidazole versus a 4-substituted benzimidazole.<sup>50</sup>

<sup>1</sup>H NMR (300 MHz,  $CDCl_3$ ):  $\delta$  = 0.94 (3H, t ( $J$  = 7.4 Hz),  $CH_3$ ), 1.71 (2H, m,  $CH_2$ ), 4.03 (2H, t ( $J$  = 6.4 Hz),  $CH_2$ ), 4.30 (2H, bs,  $NH_2$ ), 5.48 (2H, s,  $CH_2$ ), 6.62 (1H, dd ( $J$  = 1.1 Hz,  $J$  = 7.7 Hz), ArH), 7.08 (2H, m, 2ArH), 7.13 (1H, m, ArH), 7.35 (1H, s, ArH), 7.42 (1H, d ( $J$  = 8.3 Hz), ArH).

LCMS ( $ES^+$ ):  $m/z$  (%) 351 ( $M + H^+$ ), retention time 0.9 min.

HRMS ( $ES^+$ ): calcd for  $(C_{17}H_{18}Cl_2N_3O [M + H]^+)$  350.0821, found 350.0815 (1.75 ppm).

**7-Phenyl-1-(3,4-dichlorobenzyl)-1H-benzo[d]imidazol-2-amine (12).** 7-Phenyl-1H-benzo[d]imidazol-2-amine (**18**) (115 mg, 0.55 mmol), potassium hydroxide flakes (46 mg, 0.83 mmol), and 3,4-dichloro-

obenzyl chloride (113 mg, 0.58 mmol) were stirred in 8 mL of ethanol at 20 °C for 48 h. The reaction was worked up described for compound **10** and columned. Compound **12** was the more polar product obtained purified by flash column chromatography (10% methanol/dichloromethane eluent), collected as a white solid (35 mg, 18% yield). <sup>1</sup>H NMR and LCMS confirmed purity at >98%.

Absolute regiochemistry of compound **12** was confirmed by NOESY NMR: a strong interaction between CH<sub>2</sub>-dichlorobenzyl protons at 4.88 ppm (2H, s, CH<sub>2</sub>) and the ortho proton signals of the pendant phenyl ring at 7.12 ppm (2H, d, CH) was observed, indicating close proximity of these substituents. Also a crystal structure of compound **12** complex with PTR1 enzyme was obtained (Figure 9), confirming the absolute regiochemistry of compound **12** as 7-phenyl-1-(3,4-dichloro)-1H-benzo(d)imidazol-2-amine.

<sup>1</sup>H NMR (500 MHz, DMSO): δ = 4.88 (2H, s, CH<sub>2</sub>), 6.37 (1H, dd (*J* = 2.1 Hz, *J* = 8.3 Hz), ArH), 6.50 (1H, m, ArH), 6.60 (2H, s, NH<sub>2</sub>), 6.61 (1H, dd (*J* = 1.1 Hz, *J* = 7.5 Hz), ArH), 7.00 (1H, t (*J* = 7.7 Hz), ArH), 7.12 (2H, bd (*J* = 8.3 Hz), ArH), 7.21 (1H, dd (*J* = 1.1 Hz, *J* = 7.8 Hz), ArH), 7.31 (2H, t (*J* = 7.3 Hz), 2ArH), 7.38 (2H, m, 2ArH).

LCMS (ES<sup>+</sup>): *m/z* (%) 369 (M + H)<sup>+</sup>, retention time 0.9 min. HRMS (ES<sup>+</sup>): calcd for C<sub>20</sub>H<sub>16</sub>Cl<sub>2</sub>N<sub>3</sub> [M + H]<sup>+</sup> 368.0716, found 368.0708 (2.05 ppm).

**7-(*n*-Propyloxy)-1H-benzo[d]imidazol-2-amine (13).** *n*-Propyloxybenzene-1,2-diamine (**14**) (410 mg, 2.47 mmol) and cyanogenbromide 2 M solution in acetonitrile (1.36 mL, 2.72 mmol) were stirred in acetonitrile (12 mL) and water (3 mL) at 20 °C for 36 h. The mixture was then concentrated to remove the acetonitrile. Ethyl acetate (40 mL) and sodium bicarbonate solution (1 × 40 mL) were added, and the biphasic solution was transferred to a separating funnel. The organic layer was washed with water (1 × 25 mL), sodium bicarbonate solution (1 × 20 mL), and brine (2 × 30 mL), before being dried with MgSO<sub>4</sub> and concentrated to remove ethyl acetate. Crude compound **13** was purified by flash column chromatography (8% methanol/dichloromethane eluent), yielding compound **13** as a white solid (300 mg, 64% yield). <sup>1</sup>H NMR and LCMS confirmed purity at >98%.

<sup>1</sup>H NMR (500 MHz, CDCl<sub>3</sub>): δ = 1.01 (3H, t (*J* = 7.4 Hz), CH<sub>3</sub>), 1.72 (2H, m, CH<sub>2</sub>), 4.03 (2H, m, CH<sub>2</sub>), 5.83 (2H, bs, NH<sub>2</sub>), 6.46 (1H, m, ArH), 6.86 (2H, m, ArCH), 10.70 (1H, bs, NH).

LCMS (ES<sup>+</sup>): *m/z* (%) 192 (M + H)<sup>+</sup>, retention time 0.6 min. **3-Propoxybenzene-1,2-diamine (14).** 2-Nitro-6-propoxyaniline (**15**) (300 mg, 1.53 mmol) and tin(II) chloride (1.45 g, 7.65 mmol) were taken into ethanol (15 mL). The reaction was heated in a microwave reactor at 140 °C for 10 min and then poured into NaHCO<sub>3</sub> solution (30 mL) and the product was extracted into ethyl acetate (2 × 25 mL). The organic layers were combined and washed with sodium bicarbonate solution (1 × 30 mL), water (1 × 30 mL), and brine (2 × 40 mL) before being dried with MgSO<sub>4</sub> and concentrated to remove ethyl acetate. The solution was concentrated to remove ethyl acetate, affording compound **14** as a pale-yellow gum in quantitative yield. <sup>1</sup>H NMR and LCMS confirmed purity at >95%.

<sup>1</sup>H NMR (500 MHz, CDCl<sub>3</sub>): δ = 1.07 (3H, t (*J* = 7.4 Hz), CH<sub>3</sub>), 1.82 (2H, m, CH<sub>2</sub>), 3.44 (2H, m, NH<sub>2</sub>), 3.98 (2H, t (*J* = 6.5 Hz), CH<sub>2</sub>), 6.40 (2H, m, ArH), 6.68 (1H, t (*J* = 8.0 Hz), ArH).

LCMS (ES<sup>+</sup>): *m/z* (%) 167 (M + H)<sup>+</sup>, retention time 0.5 min. **2-Nitro-6-propoxyaniline (15).** 2-Amino-3-nitrophenol (500 mg, 3.23 mmol), K<sub>2</sub>CO<sub>3</sub> (669 mg, 4.84 mmol), and 3-bromopropane (438 mg, 3.35 mmol) were taken into DMF (35 mL). The reaction was stirred at 20 °C for 12 h and then poured into NaHCO<sub>3</sub> solution (20 mL), and the product was extracted into ethyl acetate (2 × 30 mL). The organic layers were combined then washed with water (1 × 30 mL), sodium bicarbonate solution (1 × 30 mL), and brine (2 × 40 mL) before being dried with MgSO<sub>4</sub> and concentrated to remove ethyl acetate. Crude compound **15** was purified by flash column chromatography (3% methanol/dichloromethane eluent), affording compound **15** as a pale-yellow solid (460 mg, 73% yield). <sup>1</sup>H NMR and LCMS confirmed purity at >98%.

<sup>1</sup>H NMR (500 MHz, CDCl<sub>3</sub>): δ = 1.09 (3H, s, CH<sub>3</sub>), 1.91 (2H, s, CH<sub>2</sub>), 4.02 (2H, m, CH<sub>2</sub>), 6.47 (2H, m, NH<sub>2</sub>), 6.64 (1H, dd (*J* = 7.8 Hz, *J* = 8.9 Hz), ArH), 6.91 (1H, d (*J* = 7.6 Hz), ArH), 7.75 (1H, dd (*J* = 1.1 Hz, *J* = 8.9 Hz), ArH).

LCMS (ES<sup>+</sup>): *m/z* (%) 197 (M + H)<sup>+</sup>, retention time 0.5 min.

**7-Chloro-1H-benzo[d]imidazol-2-amine (16).** Prepared like compound **13**, starting from 3-chlorobenzene-1,2-diamine (**17**) (624 mg, 4.38 mmol) and cyanogenbromide 2 M solution in acetonitrile (2.41 mL, 4.82 mmol), in acetonitrile (18 mL), and water (4 mL). The reaction was stirred at 20 °C for 36 h. Crude compound **16** was purified by flash column chromatography (8% methanol/dichloromethane eluent), yielding compound **16** as a white solid (510 mg, 69% yield). <sup>1</sup>H NMR and LCMS confirmed purity at >98%.

<sup>1</sup>H NMR (500 MHz, CDCl<sub>3</sub>): δ = 6.40 (2H, bs, NH<sub>2</sub>), 6.79 (1H, bm, ArH), 6.90 (1H, m, ArH), 7.0 (1H, dd (*J* = 0.8 Hz, *J* = 7.8 Hz), ArH), 10.94 (1H, bs, NH).

LCMS (ES<sup>+</sup>): *m/z* (%) 168.5 (M + H)<sup>+</sup>, retention time 0.6 min.

**3-Chlorobenzene-1,2-diamine (17).** Prepared like compound **14**, using 2-chloro-6-nitroaniline (1.0 g, 5.8 mmol), tin(II) chloride (5.5 g, 29 mmol) in ethanol 30 mL. Compound **17** was obtained in quantitative yield as a colorless gum. LCMS confirmed purity at >95%. Used as "crude" in example **16**.

LCMS (ES<sup>+</sup>): *m/z* (%) 143 (M + H)<sup>+</sup>, retention time 0.4 min.

**7-Phenyl-1H-benzo[d]imidazol-2-amine (18).** Prepared like compound **13**, starting from biphenyl-2,3-diamine (**19**) (350 mg, 1.9 mmol) and cyanogenbromide 2 M solution in acetonitrile (1.05 mL, 2.09 mmol), in acetonitrile (18 mL), and water (4 mL). The reaction was stirred at 20 °C for 18 h and worked up as described above. Crude compound **18** was purified by flash column chromatography (8% methanol/dichloromethane eluent), yielding compound **18** as a white solid (250 mg, 63% yield). <sup>1</sup>H NMR and LCMS confirmed purity at >98%.

<sup>1</sup>H NMR (500 MHz, DMSO): δ = 6.22 (2H, s, CH<sub>2</sub>), 6.95 (1H, t (*J* = 7.7 Hz), ArH), 7.08 (1H, m, ArH), 7.31 (1H, t (*J* = 7.5 Hz), ArH), 7.44 (1H, t (*J* = 7.6 Hz), ArH), 7.90 (2H, bs, NH<sub>2</sub>), 10.90 (1H, bs, NH).

LCMS (ES<sup>+</sup>): *m/z* (%) 210 (M + H)<sup>+</sup>, retention time 0.5 min.

**Biphenyl-2,3-diamine (19).** Prepared like compound **14**, using 3-phenyl-2-nitroaniline (**20**) (500 mg, 2.34 mmol), tin(II) chloride (2.2 g, 11.7 mmol) in ethanol 25 mL. The reaction was heated in a microwave reactor at 140 °C for 10 min and then worked up as previously described. The solution was concentrated to remove ethyl acetate, affording compound **19** in quantitative yield, as a colorless gum. LCMS confirmed purity at >95%. Used as "crude" in example **18**.

LCMS (ES<sup>+</sup>): *m/z* (%) 184 (M + H)<sup>+</sup>, retention time 0.5 min.

**3-Phenyl-2-nitroaniline (20).** A solution of 2-phenylnitrobenzene (398 mg, 2 mmol) and *o*-methylhydroxylamine (118 mg, 2.5 mmol) in DMF (3 mL) was added dropwise (over 5 min) to a stirred suspension of <sup>t</sup>BuOK (672 mg, 6 mmol) and Cu(I)Cl (20 mg, 0.2 mmol) in DMF (7 mL). The reaction was stirred at 20 °C for 60 min and then quenched with ammonium chloride solution. The product was extracted into DCM, dried with MgSO<sub>4</sub>, and concentrated to remove the dichloromethane. Compound **20** was separated from the side product (2-phenyl-4-nitroaniline) and remaining starting material by flash column chromatography (10% ethyl acetate/hexane eluent), affording compound **20** as a yellow solid (86 mg, 20% yield). <sup>1</sup>H NMR and LCMS confirmed purity at >98%.

<sup>1</sup>H NMR (500 MHz, CDCl<sub>3</sub>): δ = 6.5 (1H, dd (*J* = 1.3 Hz, *J* = 7.7 Hz), ArH), 6.57 (2H, s, NH<sub>2</sub>), 6.8 (1H, m, ArH), 6.89 (1H, d (*J* = 7.7 Hz), ArH), 6.95 (1H, dt (*J* = 1.2 Hz, *J* = 7.6 Hz), ArH), 7.2 (2H, m, 2ArH), 7.3 (1H, dt (*J* = 1.6 Hz, *J* = 7.7 Hz), ArH), 7.53 (1H, dd (*J* = 1.1 Hz, *J* = 7.9 Hz), ArH).

LCMS (ES<sup>+</sup>): *m/z* (%) 215 (M + H)<sup>+</sup>, retention time 0.6 min.

**Acknowledgment.** This work was funded by the Wellcome Trust (WT 077705, 082596, and 083481) and BBSRC (BBS/B/14434). We thank Scottish Enterprise and the Scottish



Structural Proteomics Facility (SSPF) for additional financial support and Openeye for free software licenses. Further, we thank Nicholas Moir for administrating the Linux workstations and Dr. Mark Agacan for maintenance of the in-house X-ray crystallography facilities.

**Supporting Information Available:** A table listing initial screening hits with corresponding percent inhibition data is available as Supporting Information. This material is available free of charge via the Internet at <http://pubs.acs.org>.

## References

- Pink, R.; Hudson, A.; Mouries, M. A.; Bendig, M. Opportunities and challenges in antiparasitic drug discovery. *Nat. Rev. Drug. Discovery* **2005**, *4*, 727–740.
- Brun, R.; Balmer, O. New developments in human African trypanosomiasis. *Curr. Opin. Infect. Dis.* **2006**, *19*, 415–420.
- Kennedy, P. G. The continuing problem of human African trypanosomiasis (sleeping sickness). *Ann. Neurol.* **2008**, *64*, 116–126.
- Nare, B.; Luba, J.; Hardy, L. W.; Beverley, S. New approaches to *Leishmania* chemotherapy: pteridine reductase 1 (PTR1) as a target and modulator of antifolate sensitivity. *Parasitology* **1997**, *114* (Suppl.), S101–S110.
- Berriman, M.; Ghedin, E.; Hertz-Fowler, C.; Blandin, G.; Renauld, H.; Bartholomeu, D. C.; Lennard, N. J.; Caler, E.; Hamlin, N. E.; Haas, B.; Bohme, U.; Hannick, L.; Aslett, M. A.; Shallom, J.; Marcello, L.; Hou, L.; Wickstead, B.; Alsmark, U. C.; Arrowsmith, C.; Atkin, R. J.; Barron, A. J.; Bringaud, F.; Brooks, K.; Carrington, M.; Cherevach, I.; Chillingworth, T. J.; Churcher, C.; Clark, L. N.; Corton, C. H.; Cronin, A.; Davies, R. M.; Doggett, J.; Djikeng, A.; Feldblyum, T.; Field, M. C.; Fraser, A.; Goodhead, I.; Hance, Z.; Harper, D.; Harris, B. R.; Hauser, H.; Hostetler, J.; Ivens, A.; Jagels, K.; Johnson, D.; Johnson, J.; Jones, K.; Kerhornou, A. X.; Koo, H.; Larke, N.; Landfear, S.; Larkin, C.; Leech, V.; Line, A.; Lord, A.; Macleod, A.; Mooney, P. J.; Moule, S.; Martin, D. M.; Morgan, G. W.; Mungall, K.; Norbertzak, H.; Ormond, D.; Pai, G.; Peacock, C. S.; Peterson, J.; Quail, M. A.; Rabbinowitsch, E.; Rajandream, M. A.; Reitter, C.; Salzberg, S. L.; Sanders, M.; Schobel, S.; Sharp, S.; Simmonds, M.; Simpson, A. J.; Tallon, L.; Turner, C. M.; Tait, A.; Tivey, A. R.; Van Aken, S.; Walker, D.; Wanless, D.; Wang, S.; White, B.; White, O.; Whitehead, S.; Woodward, J.; Wortman, J.; Adams, M. D.; Embley, T. M.; Gull, K.; Ullu, E.; Barry, J. D.; Fairlamb, A. H.; Opperdoes, F.; Barrell, B. G.; Donelson, J. E.; Hall, N.; Fraser, C. M.; Melville, S. E.; El-Sayed, N. M. The genome of the African trypanosome *Trypanosoma brucei*. *Science* **2005**, *309*, 416–422.
- Gangjee, A.; Jain, H. D.; Kurup, S. Recent advances in classical and non-classical antifolates as antitumor and antiopportunistic infection agents: part I. *Anticancer Agents Med. Chem.* **2007**, *7*, 524–542.
- Gangjee, A.; Jain, H. D.; Kurup, S. Recent advances in classical and nonclassical antifolates as antitumor and antiopportunistic infection agents: Part II. *Anticancer Agents Med. Chem.* **2008**, *8*, 205–231.
- Bello, A. R.; Nare, B.; Freedman, D.; Hardy, L.; Beverley, S. M. PTR1: a reductase mediating salvage of oxidized pteridines and methotrexate resistance in the protozoan parasite *Leishmania major*. *Proc. Natl. Acad. Sci.* **1994**, *91*, 11442–11446.
- Sienkiewicz, N.; Jaroslowski, S.; Wyllie, S.; Fairlamb, A. H. Chemical and genetic validation of dihydrofolate reductase-thymidylate synthase as a drug target in African trypanosomes. *Mol. Microbiol.* **2008**, *69*, 520–533.
- Nare, B.; Hardy, L. W.; Beverley, S. M. The roles of pteridine reductase 1 and dihydrofolate reductase-thymidylate synthase in pteridine metabolism in the protozoan parasite *Leishmania major*. *J. Biol. Chem.* **1997**, *272*, 13883–13891.
- Cunningham, M. L.; Titus, R. G.; Turco, S. J.; Beverley, S. M. Regulation of differentiation to the infective stage of the protozoan parasite *Leishmania major* by tetrahydrobiopterin. *Science* **2001**, *292*, 285–287.
- Cavazzuti, A.; Paglietti, G.; Hunter, W. N.; Gamarro, F.; Piras, S.; Loriga, M.; Allecca, S.; Corona, P.; McLuskey, K.; Tulloch, L.; Gibellini, F.; Ferrari, S.; Costi, M. P. Discovery of potent pteridine reductase inhibitors to guide antiparasitic drug development. *Proc. Natl. Acad. Sci.* **2008**, *105*, 1448–1453.
- Hardy, L. W.; Matthews, W.; Nare, B.; Beverley, S. M. Biochemical and Genetic Tests for Inhibitors of *Leishmania Pteridine* Pathways. *Exp. Parasitol.* **1997**, *87*, 158–170.
- Ecker, G. F.; Noe, C. R. In silico prediction models for blood–brain barrier permeation. *Curr. Med. Chem.* **2004**, *11*, 1617–1628.
- Dawson, A.; Gibellini, F.; Sienkiewicz, N.; Tulloch, L. B.; Fyfe, P. K.; McLuskey, K.; Fairlamb, A. H.; Hunter, W. N. Structure and reactivity of *Trypanosoma brucei* pteridine reductase: inhibition by the archetypal antifolate methotrexate. *Mol. Microbiol.* **2006**, *61*, 1457–1468.
- Gourley, D. G.; Schuttelkopf, A. W.; Leonard, G. A.; Luba, J.; Hardy, L. W.; Beverley, S. M.; Hunter, W. N. Pteridine reductase mechanism correlates pterin metabolism with drug resistance in trypanosomatid parasites. *Nat. Struct. Biol.* **2001**, *8*, 521–525.
- Congreve, M.; Chessari, G.; Tisi, D.; Woodhead, A. J. Recent Developments in Fragment-Based Drug Discovery. *J. Med. Chem.* **2008**, *51*, 3661–3680.
- Hajduk, P. J.; Greer, J. A decade of fragment-based drug design: strategic advances and lessons learned. *Nat. Rev. Drug. Discovery* **2007**, *6*, 211–219.
- Brenk, R.; Schipani, A.; James, D.; Krasowski, A.; Gilbert, I. H.; Frearson, J.; Wyatt, P. G. Lessons learned from assembling screening libraries for drug discovery for neglected diseases. *ChemMedChem* **2008**, *3*, 435–444.
- Lorber, D. M.; Shoichet, B. K. Flexible ligand docking using conformational ensembles. *Protein Sci.* **1998**, *7*, 938–950.
- Wei, B. Q.; Baase, W. A.; Weaver, L. H.; Matthews, B. W.; Shoichet, B. K. A model binding site for testing scoring functions in molecular docking. *J. Mol. Biol.* **2002**, *322*, 339–355.
- Hopkins, A. L.; Groom, C. R.; Alex, A. Ligand efficiency: a useful metric for lead selection. *Drug Discovery Today* **2004**, *9*, 430–431.
- Schuttelkopf, A. W.; Hardy, L. W.; Beverley, S. M.; Hunter, W. N. Structures of *Leishmania major* Pteridine Reductase Complexes Reveal the Active Site Features Important for Ligand Binding and to Guide Inhibitor Design. *J. Mol. Biol.* **2005**, *352*, 105–116.
- Chen, H.; Lyne, P. D.; Giordanetto, F.; Lovell, T.; Li, J. On evaluating molecular-docking methods for pose prediction and enrichment factors. *J. Chem. Inf. Model.* **2006**, *46*, 401–415.
- McGaughey, G. B.; Sheridan, R. P.; Bayly, C. I.; Culbertson, J. C.; Kreatsoulas, C.; Lindsley, S.; Maiorov, V.; Truchon, J. F.; Cornell, W. D. Comparison of Topological, Shape, and Docking Methods in Virtual Screening. *J. Chem. Inf. Model.* **2007**, *47*, 1504–1519.
- Tan, L.; Geppert, H.; Sisay, M. T.; Gutschow, M.; Bajorath, J. Integrating Structure- and Ligand-Based Virtual Screening: Comparison of Individual, Parallel, and Fused Molecular Docking and Similarity Search Calculations on Multiple Targets. *ChemMedChem* **2008**, *3*, 1566–1571.
- von Korff, M.; Freyss, J.; Sander, T. Comparison of Ligand- and Structure-Based Virtual Screening on the DUD Data Set. *J. Chem. Inf. Model.* **2009**, *49*, 209–231.
- Verdonk, M. L.; Berdini, V.; Hartshorn, M. J.; Mooij, W. T.; Murray, C. W.; Taylor, R. D.; Watson, P. Virtual screening using protein–ligand docking: avoiding artificial enrichment. *J. Chem. Inf. Comput. Sci.* **2004**, *44*, 793–806.
- Marcou, G.; Rognan, D. Optimizing fragment and scaffold docking by use of molecular interaction fingerprints. *J. Chem. Inf. Model.* **2007**, *47*, 195–207.
- Mpamhanga, C. P.; Chen, B.; McLay, I. M.; Willett, P. Knowledge-based interaction fingerprint scoring: a simple method for improving the effectiveness of fast scoring functions. *J. Chem. Inf. Model.* **2006**, *46*, 686–698.
- Klebe, G. Virtual ligand screening: strategies, perspectives and limitations. *Drug Discovery Today* **2006**, *11*, 580–594.
- Mancera, R. L. Molecular modeling of hydration in drug design. *Curr. Opin. Drug Discovery Dev.* **2007**, *10*, 275–280.
- Sousa, S. F.; Fernandes, P. A.; Ramos, M. J. Protein–ligand docking: current status and future challenges. *Proteins* **2006**, *65*, 15–26.
- Babaoglu, K.; Shoichet, B. K. Deconstructing fragment-based inhibitor discovery. *Nat. Chem. Biol.* **2006**, *2*, 720–723.
- Hajduk, P. J. Puzzling through fragment-based drug design. *Nat. Chem. Biol.* **2006**, *2*, 658–659.
- Brenk, R.; Vetter, S. W.; Boyce, S. E.; Goodin, D. B.; Shoichet, B. K. Probing molecular docking in a charged model binding site. *J. Mol. Biol.* **2006**, *357*, 1449–1470.
- Gerber, P. R. Charge distribution from a simple molecular orbital type calculation and nonbonding interaction terms in the force field MAB. *J. Comput.-Aided. Mol. Des.* **1998**, *12*, 37–51.
- Gerber, P. R.; Muller, K. MAB, a generally applicable molecular force field for structure modelling in medicinal chemistry. *J. Comput.-Aided. Mol. Des.* **1995**, *9*, 251–268.



- (39) Ertl, P.; Rohde, B.; Selzer, P. Fast calculation of molecular polar surface area as a sum of fragment-based contributions and its application to the prediction of drug transport properties. *J. Med. Chem.* **2000**, *43*, 3714–3717.
- (40) Kuzmic, P.; Sideris, S.; Cregar, L. M.; Elrod, K. C.; Rice, K. D.; Janc, J. W. High-throughput screening of enzyme inhibitors: automatic determination of tight-binding inhibition constants. *Anal. Biochem.* **2000**, *281*, 62–67.
- (41) Leslie, A. G. The integration of macromolecular diffraction data. *Acta Crystallogr., Sect. D: Biol. Crystallogr.* **2006**, *62*, 48–57.
- (42) Evans, P. Scaling and assessment of data quality. *Acta Crystallogr., Sect. D: Biol. Crystallogr.* **2006**, *62*, 72–82.
- (43) Collaborative Computational Project Number 4. The CCP4 suite: programs for protein crystallography. *Acta Crystallogr., Sect. D: Biol. Crystallogr.* **1994**, *50*, 760–763.
- (44) Otwinowski, Z.; Minor, W. Processing of X-ray Diffraction Data Collected in Oscillation Mode. In *Methods in Enzymology*; Carter, C. W. J., Sweet, R. M., Eds.; Academic Press: New York, 1997; Vol. 276, pp 307–326.
- (45) Vagin, A.; Teplyakov, A. MOLREP: an automated program for molecular replacement. *J. Appl. Crystallogr.* **1997**, *30*, 1022–1025.
- (46) Murshudov, G. N.; Vagin, A. A.; Dodson, E. J. Refinement of macromolecular structures by the maximum-likelihood method. *Acta Crystallogr., Sect. D: Biol. Crystallogr.* **1997**, *53*, 240–255.
- (47) Winn, M. D.; Isupov, M. N.; Murshudov, G. N. Use of TLS parameters to model anisotropic displacements in macromolecular refinement. *Acta Crystallogr., Sect. D: Biol. Crystallogr.* **2001**, *57*, 122–133.
- (48) Schuttelkopf, A. W.; van Aalten, D. M. F. PRODRG: a tool for high-throughput crystallography of protein–ligand complexes. *Acta Crystallogr., Sect. D: Biol. Crystallogr.* **2004**, *60*, 1355–1363.
- (49) Emsley, P.; Cowtan, K. Coot: model-building tools for molecular graphics. *Acta Crystallogr., Sect. D: Biol. Crystallogr.* **2004**, *60*, 2126–2132.
- (50) Iemura, R.; Hori, M.; Ohtaka, H. Syntheses of the Metabolites of 1-(2-Ethoxyethyl)-2-(Hexahydro-4-Methyl-1*h*-1,4-Diazepin-1-Yl)-1*h*-Benzimidazole Difumarate (kg-2413) and Related Compounds. *Chem. Pharm. Bull.* **1989**, *37*, 962–966.